International Journal of Heat and Mass Transfer 100 (2016) 303–319

Contents lists available at ScienceDirect

International Journal of Heat and Mass Transfer

journal homepage: www.elsevier.com/locate/ijhmt

Fluid–solid interaction in natural convection heat transfer in a square cavity with a perfectly thermal-conductive flexible diagonal partition

Esmail Jamesahar [a], Mohammad Ghalambaz [a,*], Ali J. Chamkha [b,c]

[a] Department of Mechanical Engineering, Dezful Branch, Islamic Azad University, Dezful, Iran
[b] Mechanical Engineering Department, Prince Mohammad Bin Fahd University, P.O. Box 1664, Al-Khobar 31952, Saudi Arabia
[c] Prince Sultan Endowment for Energy and Environment, Prince Mohammad Bin Fahd University, P.O. Box 1664, Al-Khobar 31953, Saudi Arabia

ARTICLE INFO

Article history:
Received 10 October 2015
Received in revised form 13 March 2016
Accepted 14 April 2016

Keywords:
Fluid-structure interaction
Unsteady natural convection
Flexible highly conductive plate

ABSTRACT

The unsteady natural convective heat transfer of an incompressible fluid is studied in a square cavity divided into two triangles using a flexible thermal conductive membrane. The temperature difference in the cavity induces buoyancy forces and natural convective flows. The membrane is adopted to be very flexible and thin, and hence, the interaction of the fluid and solid structure interaction (FSI) could change the shape of the membrane. An arbitrary Lagrangian–Eulerian (ALE) formulation associated with an unstructured grid is utilized to formulate the motion of the membrane. The solid and fluid governing equations are formulated and written in a non-dimensional form and the behavior of the membrane and the convective heat transfer of the cavity for various non-dimensional parameters are examined. The effects of the stiffness of the membrane and the fluid parameters on the shape of the membrane and the convective heat transfer in the cavity are studied.

1. Introduction

The natural convective heat transfer has been the subject of many studies due to its prime importance in various industrial and natural processes. Some of the practical applications of natural convection in enclosures are solar collectors, cooling of electronic equipment, energy storage systems, air conditioned system in buildings, thermal insulation and fire propensity control in buildings [1–3].

Giving the popularity of the natural convection heat transfer in a differentially heated cavity, this problem has been addressed as a benchmark study in many of the previous studies [3,5–15].

Earlier investigators have theoretically and experimentally addressed many aspects of convective heat transfer in cavity enclosures involving conjugate heat transfer effects [16], nanofluids and entropy generation [17], magnetic field effects [18], cavity filled with porous media [19] and the presence of a solid partition [20].

Many researchers have studied different geometry aspects of convective heat transfer in simple enclosures, such as the geometry of triangular shape [21], C-shape [22], concentric annulus [23], hemispherical shape [24–26], and parallelogrammic shape [27].

Modeling of real systems may differ distinctly from a simple enclosure. For example, a box containing electronic units is divided into partitions using thermal conductive plates. Some of sensitive electronic equipment should be insulated from the surrounding using a conductive metallic cover. In many cases, a chemical reactor should be divided in sections in which each section contains different chemical species, but the heat transfer could be occurred between the species through partitions. In a solar collector, the convection in the two adjacent air layers is coupled at the glazing. There are applications in which two fluids or containment gases are separated by a very thin flexible layer. In building insulation applications, the cavity in the walls is filled with a layer of polyethylene to prevent heat loss. For the case of a very thin membrane layer, the membrane is completely flexible and can go under deflection through the interaction of the structure with the free convection flow. Hence, the practical application of partitions in enclosures has encouraged researchers to examine the effect of the presence of partitions on convective heat transfer in cavities.

Tatsuo et al. [20] have experimentally studied the effect of the presence of a partition on the steady-state natural convective heat transfer in a cavity with a differential difference temperature at the sidewalls. Acharya and Jetli [28] have numerically studied the effect of the presence of a vertical partition on the natural convective heat transfer in a cavity with differentially difference sidewalls temperature. Nishimura et al. [14] have addressed the effect of the presence of multiple vertical partitions on the convective heat

---

* Corresponding author. Tel.: +98 916 644 2671; fax: +98 (61) 42420601.

E-mail addresses: behravan.jam@gmail.com (E. Jamesahar), m.ghalambaz@iaud.ac.ir (M. Ghalambaz), achamkha@pmu.edu.sa (A.J. Chamkha).

http://dx.doi.org/10.1016/j.ijheatmasstransfer.2016.04.046
0017-9310/

Nomenclature

Latin symbols

d	displacement
E	Young's modulus
E_τ	dimensionless flexibility
f_i	dimensionless body force
f_p	dimensionless body force
F_v	dimensionless body force
g	gravitational acceleration vector
Gr	Grashof number
k	thermal conductivity
L	cavity size
Nu	Nusselt number
p	dimensionless pressure
Pr	Prandtl number
Ra	thermal Rayleigh number
t	dimensionless time
T	temperature
T_0	initial average of the temperature in the enclosure
U	dimensionless velocity magnitude
u, v	dimensionless velocity vector
u_p	moving coordinate velocity
W_s	strain energy density
x, y	Cartesian coordinates

Greek symbols

μ_l	Lamé parameter
α	thermal diffusivity
β	thermal expansion coefficient
ε	strain
θ	dimensionless temperature
κ	solid-to-fluid thermal conductivity ratio
λ	Lamé parameters
ν	kinematic viscosity
ρ	density
σ	stress tensor
υ	Poisson's ratio
τ	Dimensionless time

Subscripts

c	cold
f	fluid
h	hot
p	partition
R	ratio

Superscripts

$*$	dimensional

transfer in a rectangular enclosure. Kahveci [4] has examined the effect of the presence of a vertical partition with finite thermal conductivity on the natural convective heat transfer in a square cavity. Chamkha and Ben-Nakhi [12,29,30] and Cheikh et al. [31] have numerically examined the effect of partial partitions (fins) on the convective heat transfer in cavities. All of the mentioned studies have addressed the effect of the presence of a partition on the steady state convective heat transfer in an enclosure.

Recently, there are few studies which have addressed the unsteady convective heat transfer in portioned enclosures. Suvash and Gu [32], Suvash et al. [33] have studied the unsteady natural convective heat transfer in a triangular cavity. Xu et al. [13] have examined the unsteady natural convective heat transfer of air in a square cavity with a highly conductive vertical partition.

In all of the studies mentioned in the literature, the partition has been considered as rigid. However, in many of real world problems, the partition can be flexible and the fluid-structure interaction (FSI) can change the shape of the partition. Consequently, the shape of the partition can affect the flow and heat transfer in the cavity. In the transient case, the motion of the flexible partition, the fluid flow and the heat transfer are coupled.

To the best of authors' knowledge, the effect of the presence of a flexible partition in a cavity on the natural convective heat transfer neither in the steady state nor in the unsteady state has been addressed yet. The present study aims to examine the effect of the presence of a perfectly conductive flexible partition on the natural convective heat transfer in a square cavity.

2. Mathematical formulation

Consider the laminar flow steady-state natural convection heat transfer of a Newtonian fluid in a square cavity of size L (height H and length L where $L \approx H$). The cavity is divided into two triangular partitions using a diagonal thin flexible membrane of thickness t_p^*. The membrane is flexible with the Young's modulus of E, Poison's ratio ν and density ρ. The vertical walls of the cavity are isothermal of temperature difference ΔT while the top and bottom walls are perfectly insulated. There is a very small open boundary with the relative pressure of zero in each partition, allowing fluid entrance or ejection due to movement of the membrane and the change of volume of the partitions. The size of the open boundary is 0.1% of the height of the cavity. It is assumed that the membrane is very thin and perfectly thermally conductive with very low thermal capacity. Hence, the effect of temperature gradients and transient energy storage in the plate are neglected. It is assumed that the temperature difference between the cavity sidewalls is limited, and hence, the thermo-physical properties are independent of temperature variation and the Boussinesq approximation is applicable. The body force due to the weight of the membrane and the buoyancy forces are taken into account. A schematic representation of the cavity, coordinate system and the physical model are depicted in Fig. 1.

The governing equations for the geometrically nonlinear elastodynamic structural displacement of the membrane can be written as:

$$\rho_s \frac{d^2 \boldsymbol{d}_s^*}{dt^2} - \nabla \boldsymbol{\sigma}^* = \boldsymbol{F}_v^* \tag{1}$$

The governing equations of the conservation of mass, momentum and energy in arbitrary Lagrangian–Eulerian (ALE) formulation are written as:

$$\nabla \cdot \boldsymbol{u}^* = 0 \tag{2}$$

$$\frac{\partial \boldsymbol{u}^*}{\partial t} + (\boldsymbol{u}^* - \boldsymbol{w}^*).\nabla \boldsymbol{u}^* = -\frac{1}{\rho_f}\nabla P^* + \nu_f \nabla^2 \boldsymbol{u}^* + \beta \boldsymbol{g}(T - T_c) \tag{3}$$

$$\frac{\partial T}{\partial t} + (\boldsymbol{u}^* - \boldsymbol{w}^*).\nabla T = \alpha_f \nabla^2 T^* \tag{4}$$

where $\boldsymbol{\sigma}^*$ is the stress tensor, $\boldsymbol{d}_s^*$ is the solid displacement vector, $\boldsymbol{F}_v^*$ is the applied body force per unit of area, including the weight of the membrane and the buoyancy forces acting on the flexible membrane, $\boldsymbol{u}^*$ is the fluid velocity vector, $\boldsymbol{w}^*$ is the moving coordinate velocity, P^* is the fluid pressure and T is the fluid temperature.

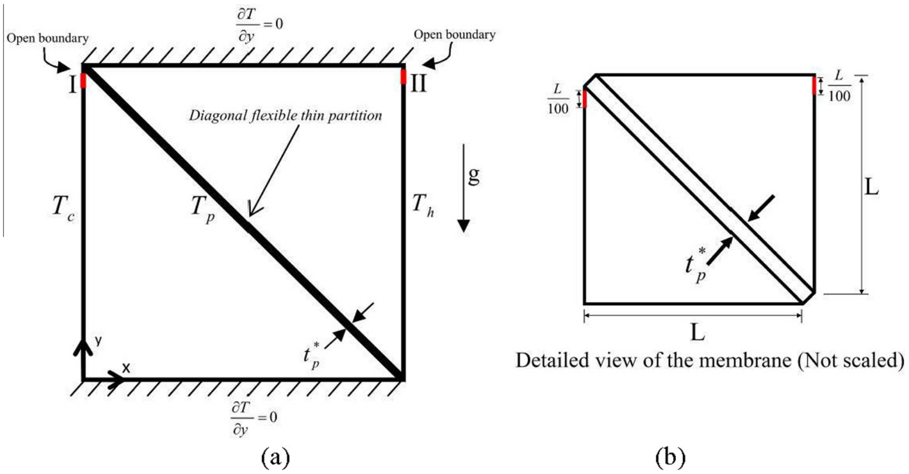

Fig. 1. A schematic representation of the cavity with a diagonal partition. (a) Physical details and (b) geometry details.

The density of the solid and fluid are respectively denoted by ρ_s and ρ_f. Here, α_f and υ_f represent the thermal diffusivity and kinematic viscosity of the fluid, respectively, $\boldsymbol{g} = (0, g_y)$ is the gravitational acceleration constant, and β is volumetric thermal expansion coefficient.

Considering the membrane as a simple hyper-elastic material and using the Neo-Hookean model and by taking into account the nonlinear geometry effects, the stress tensor σ is written as

$$\sigma = \boldsymbol{J}^{-1}\boldsymbol{FSF}^T \tag{5}$$

where $\boldsymbol{F} = (\boldsymbol{I} + \nabla \boldsymbol{d}_s^*)$ and $\boldsymbol{J} = \det(\boldsymbol{F})$ and $\mathbf{S} = \partial \boldsymbol{W}_s / \partial \boldsymbol{\varepsilon}$ in which $\boldsymbol{W}_s$ is the strain energy density function and ε is the strain, which they are defined as:

$$\boldsymbol{W}_s = \frac{1}{2}\mu_l(\boldsymbol{J}^{-1}\boldsymbol{I}_1 - 3) - \mu_l \ln(\boldsymbol{J}) + \frac{1}{2}\lambda(\ln(\boldsymbol{J}))^2 \tag{6}$$

$$\boldsymbol{\varepsilon} = \frac{1}{2}(\nabla \boldsymbol{d}_s^* + \nabla \boldsymbol{d}_s^{*T} + \nabla \boldsymbol{d}_s^{*T} \nabla \boldsymbol{d}_s^*) \tag{7}$$

where $\boldsymbol{I}_1$ is the first invariant of the right Cauchy–Green deformation tensor. The coefficients of μ_l and λ are Lamé parameters evaluated as $\mu_l = E/(2(1 + v))$ and $\lambda = Ev/[(1 + v)(1 - 2v)]$. It should be noted that the utilized model of Neo-Hookean is usable for modeling materials such as plastics and rubber-like membranes [34].

Here, it is assumed that the membrane is isotropic and uniform. The no-slip boundary condition between the fluid and walls is assumed. It is also assumed that the walls and the membrane are impermeable. The left wall is at the constant temperature of T_c and the right wall is at the constant temperature of T_h, while the top and bottom walls are insulated. The boundary conditions for the fluid–solid interaction at the plate surfaces are continuity of kinematic forces and dynamic movements. Considering the regular no-slip boundary condition for the fluid at the solid interface results in:

$$\frac{\partial \boldsymbol{d}_s^*}{\partial t} = \boldsymbol{u}^* \text{ and } \boldsymbol{\sigma}^* \cdot \boldsymbol{n} = (-P^*\boldsymbol{I} + \mu_f(\nabla \boldsymbol{u}^* + \nabla \boldsymbol{u}^{*T})) \cdot \boldsymbol{n} \tag{8}$$

For the energy equation, the energy balance for the highly conductive plate gives:

$$T^+ = T^- \tag{9}$$

where the + and – indicate the upside and downside of the plate. The plate at the corners is assumed to be clamped with $\frac{\partial \boldsymbol{d}_s^*}{\partial t} = 0$. The constant pressure point, the same as those utilized in previous studies regarding to natural convection heat transfer studies inside solid enclosures, induces a significant computational error as it is not possible to maintain the pressure at such a point constant without leaking some mass from the point. Indeed, the presence of opening boundaries is crucial for the present study. Otherwise, a variable pressure constraint inside each enclosure is required to keep the continuation equations satisfied. As many of enclosures are not fixed and can leak a small amount of mass from some small holes. We have utilized the open boundaries of *I* and *II* to allow mass balance in the cavity in a rational way. Thus, at the right and left walls, the open boundaries (indicated by *II* and *I* depicted in Fig. 1) are as follows:

$$[-p + \mu \nabla \boldsymbol{u}^*].\boldsymbol{n} = 0 \tag{10}$$

where the gauge pressure outside the cavity is considered zero. As the size of the open boundaries is very small, the possible tensions between the fluid inside the cavity and the fluid outside the cavity are neglected for convenience.

For the initial conditions, it is assumed that the triangular enclosure connected to the hot and cold walls are respectively at uniform temperatures of T_h and T_c. The membrane is at rest without any tension with the temperature of $(T_h + T_c)/2$ and the fluid in both enclosures is quiescent (i.e. $\boldsymbol{u}^*=0$). Now, using the following non-dimensional parameters:

$$\boldsymbol{d}_s = \frac{\boldsymbol{d}_s^*}{L}, \quad \boldsymbol{\sigma} = \frac{\boldsymbol{\sigma}^*}{E}, \quad \tau = \frac{t\alpha_f}{L^2}, \quad (x, y) = \frac{(x^*, y^*)}{L}, \tag{11a}$$

$$(\boldsymbol{u}, \boldsymbol{v}) = \frac{(\boldsymbol{u}^*, \boldsymbol{v}^*)L}{\alpha_f}, \quad \boldsymbol{w} = \frac{\boldsymbol{w}^* L}{\alpha_f}, \quad P = \frac{L^2}{\rho_f \alpha_f^2}P^*, \quad \theta = \frac{T - T_c}{T_h - T_c}. \tag{11b}$$

The governing equations (1)–(4) are written in the following non-dimensional form

$$\frac{1}{\rho_R}\frac{d^2 \boldsymbol{d}_s}{d\tau^2} - E_\tau \nabla \boldsymbol{\sigma} = E_\tau \boldsymbol{F}_v \tag{12}$$

$$\nabla \cdot \boldsymbol{u} = 0 \tag{13}$$

$$\frac{\partial \boldsymbol{u}}{\partial t} + (\boldsymbol{u} - \boldsymbol{w}).\nabla \boldsymbol{u} = -\nabla P + Pr\nabla^2 \boldsymbol{u} + Pr.Ra\theta \tag{14}$$

$$\frac{\partial \theta}{\partial t} + (\boldsymbol{u} - \boldsymbol{w}).\nabla \theta = \nabla^2 \theta \tag{15}$$

by using the following non-dimensional parameters:

$$Ra = \frac{\boldsymbol{g}_y\beta(T_h - T_c)L^3}{\upsilon_f\alpha_f}, \quad Pr = \frac{\upsilon_f}{\alpha_f}, \quad E_\tau = \frac{EL^2}{\rho_f\alpha_f^2},$$
$$\boldsymbol{F}_\upsilon = \frac{(\rho_f - \rho_s)L\boldsymbol{g}_y}{E}, \quad \rho_R = \frac{\rho_f}{\rho_s} \tag{16}$$

In the above equation, Ra and Pr are the Rayleigh and Prandtl numbers, respectively. E_τ and $\boldsymbol{F}_v$ are the flexibility and body force parameters, and ρ_R is the density ratio parameter. Here, $\boldsymbol{g}_y$ is in the y direction, denoting the gravity acceleration constant. The positive direction of $\boldsymbol{g}_y$ is shown in Fig. 1. It should be noted that $\boldsymbol{F}_v$ which denotes the non-dimensional body force is positive when the density of the membrane is lower than the density of the fluid inside the cavity. In this case, the body force is positive and tends to move the membrane upward. The non-dimensional thickness of the membrane is also $t_p = t^*_p/L$. The boundary conditions are also written in the following non-dimensional forms:

$\theta = 0$ at the cold wall, $\theta = 1$ at the hot wall, $\partial\theta/\partial\boldsymbol{n} = 0$ at top and bottom walls

$$\theta^+ = \theta^- \text{ for the membrane} \tag{17}$$

The solid–fluid interaction boundary conditions are also written as:

$$\frac{\partial \boldsymbol{d}_s}{\partial\tau} = \boldsymbol{u} \text{ and } E_\tau \cdot \boldsymbol{\sigma} \cdot \boldsymbol{n} = (-P\boldsymbol{I} + Pr(\nabla\boldsymbol{u} + \nabla\boldsymbol{u}^T)) \cdot \boldsymbol{n} \tag{18}$$

The non-dimensional initial temperature sat the cold and hot enclosures are respectively as $\theta = 0$ and $\theta = 1$, the plate is also at $\theta = 0.5$. The non-dimensional initial velocity is $\boldsymbol{u} = 0$.

At the open boundaries of II and I, the following non-dimensional relation is also considered:

$$[-P + Pr\nabla\boldsymbol{u}].\boldsymbol{n} = 0 \tag{19}$$

In the present study, the parameter of interest is the Nusselt number, which shows the heat transfer from the wall. The local Nusselt number is written as:

$$Nu_l = hy/k_f \text{ at } x = 0 \tag{20}$$

where h is the local convective heat transfer coefficient at the wall. Using energy balance at the wall gives $h(T_h - T_c) = -k_f\frac{\partial T}{\partial x^*}$ where invoking the non-dimensional parameters results in:

$$Nu_l = -\frac{\partial\theta}{\partial x} \text{ at } x = 0 \tag{21}$$

The average Nusselt number at the wall is also introduced as:

$$Nu = \int_0^1 Nu_l dy \tag{22}$$

As a practical case study, the fluid in the partition is adopted as liquid water. The constructive material of the membrane adopted as polyethylene (LPDE). The thermophysical properties and the corresponding dimensionless parameters for the fluid and membrane and the governing equations are summarized in Table 1.

Based on the results of Table 1, the default values of the non-dimensional parameters for non-dimensional study of the problem are considered as Ra = 1.0E7, Pr = 6.0, E_τ = 1.4E16 and F_v = 1.6E−2 in this paper otherwise the value of the non-dimensional parameter will be stated.

3. Numerical method and validation

3.1. Numerical method

The system of partial differential equations (PEDs), Eqs. (10)–(13), subject to the described boundary conditions, is transformed into the weak form and solved numerically in the moving grid system of ALE using the Galerkin finite element method [35]. A non-uniform unstructured grid associated with boundary layer grids is utilized. A schematic view of the utilized grid is depicted in Fig. 3. The quality of the gird is also monitored at each time step during the deformation of the membrane to maintain it high. A re-meshing procedure is commenced to enhance the quality of the utilized grid. In this regard, when the maximum element distortion reaches above 20, the solver is stopped temporarily, and the solution data are stored in the memory. Then, a new mesh is generated in the system geometry including the deformed fin. Finally, the solution is interpolated back in the new mesh and the computations are continued. The re-meshing procedure is required only for large oscillating fin frequencies of about $A \sim 0.1$. The Bi-quadratic functions and the three-point Gaussian quadrature was utilized for evaluating the residuals. Then, the Newton–Raphson method was employed to solve the residual equations iteratively. The computations were terminated when the error became below 10^{-5} in each time step. An automatic time step procedure is also utilized to avoid divergence of the solution and maintain the solution accurate. The details of discretization of the governing equations and the numeric procedure can be found in Donea and Huerta [35] and Zienkiewicz et al. [36].

The solution procedure was successfully validated against the study of Deng and Tang [5], Anandalakshmi and Tanmay [6], Vahl Davis [7], Shi and Khodadahi [8], Sathiyamoorthy and Chamkha [9], Nag et al. [10] Kaminski and Prakash [11], Chamkha and Ben-Nakhi [12], Kahveci [4], Xu et al. [13], Nishimura [14] and Küttler and Wall [15]. Details of some of the comparisons will be described in the next section.

It is clear that as the Rayleigh number increases, the velocity gradients and the buoyancy forces in the vicinity of the walls and solid surfaces increase. Therefore, as the Rayleigh number rises, a finer grid size is needed to capture the higher field gradients. Thus, the grid check was performed for the highest Rayleigh number ($Ra \approx 10^7$), which was adopted in the present study. Different grid sizes in cases of 1–4 are selected. The results for non-dimensional velocity of fluid at point A with the geometrical coordinates of x = 0.4845, y = 0.4845 next to the membrane and the average Nusselt number at different time steps are reported in Table 2 when $Ra = 1.0047 \times 10^7$ and Pr = 5.48. As seen, the grid size of Case 3 provides acceptable results. The effect of the grid size on the temperature time series for point A is plotted in Fig. 2. This figure also confirms that the Grid size of Case 3 could provide accurate results.

Table 1
Physical and thermal properties of materials for the case study when L = 1 m, $T_h - T_c$ = 1 K and t_p = 2.4E−5.

Material	Physical properties	Unit	Thermal properties	Unit	Dimensionless parameters
Fluid	ρ_f = 996.59	kg/m^3	α = 1.4627e−7	m^2/s	Ra = 1.005E7
			k = 0.609	W/m.K	Pr = 5.476
	μ = 0.852e−3	Pa.s	C_p = 4179	J/kg.K	E_τ = 1.407E16
			β = 1.2E-7	1/K	F_v = 1.646E−2
Membrane	E = 3E5	Pa	k = 1000	J/kg.K	
	ρ_s = 1500	kg/m^3	C_p = 100	W/m.K	

Table 2
Non-dimensional velocity magnitude of fluid (U) and average Nusselt (Nu) for the steady state solution when $Pr = 5.48$ and $Ra = 1.0048 \times 10^7$ (the case of rigid membrane).

Cases	Domain elements	Velocity (U)*	Average Nusselt
Case 1	3736	485.67	8.65
Case 2	13,048	473.54	8.92
Case 3	16,970	475.01	8.93
Case 4	25,156	475.08	8.93

* $U = \sqrt{u^2 + v^2}$.

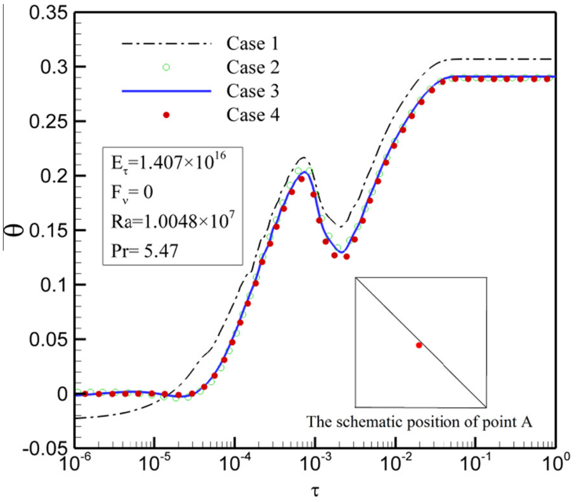

Fig. 2. Time series for the temperature at point A ($x = 0.4845$, $y = 0.4845$) calculated in different grids.

Hence, in the further calculations the grid size of Case 3 was selected. A view of the utilized grid is illustrated in Fig. 3.

3.2. Validation

As a first case for validation, the results of the present study are compared with the steady-state results of the natural convection in a simple rigid square cavity available in the literature. In this case, the regular cavity without a partition is considered while the top and bottom walls of the cavity are insulated and the sidewalls are isothermal and subject to a temperature difference. As the open boundary in the cavity of the present study is very small, the presence of such small open boundaries near the top corners (i.e. *I* and *II* depicted in Fig. 1) did not affect the solution. Indeed, these open boundaries act as pressure reference points for the regular cavity. The steady-state results in the present study are obtained using a transient solution of the problem after elapsing of long times when the solution reaches its steady-state situation. The comparisons between the results of the present study and the results reported by Deng and Tang [5], Anandalakshmi and Tanmay [6], Vahl Davis [7], Shi and Khodadahi [8], Sathiyamoorthy and Chamkha [9], Nag et al. [10] are shown in Table 3. As seen, there is excellent agreement with the results of the present study and the previous studies.

As a second case for validation, conjugate natural convection in a square cavity is investigated. For this purpose, results of the present study are compared with the results addressed by Kaminski and Prakash [11]. In the study of Kaminski and Prakash, the steady state conjugate natural convection in a square cavity is studied when the top and bottom walls of the cavity are insulated and the sidewalls are at different constant temperatures of T_c and T_h. Kaminski and Prakash considered a finite thickness and finite thermal conductivity for one of the side walls of the cavity while the other three walls are taken to be of zero thickness. In the study of Kaminski and Prakash, the dimensionless parameter of thermal conductivity ratio (κ) is defined as the ratio of the solid to the fluid thermal conductivities coefficients (k_s/k_f). The comparison between the results of the present study and the results reported by Kaminshi and Prakash for the average Nusselt number at various Grashof numbers ($Gr = Ra \times Pr$) is shown in Table 4. As seen, there is excellent agreement between the results of the present study and the results reported by Kaminski and Prakash.

In the next step, a comparison between the results of the present study and those reported by Ben-Nakhi and Chamkha [12] is performed in Fig. 4. Ben-Nakhi and Chamkha has studied the conjugate natural convection in a square cavity with an inclined thin fin at the hot wall. The fin is attached to the left hot thin wall while the other walls are thick with finite thermal conductivity. The left wall is assumed to be heated while the external sides of other three walls are assumed to be cold. In Fig. 4, a comparison between the results of the present study and the contour maps of the isotherms (θ) and streamlines (ψ) reported by Ben-Nakhi and Chamkha is

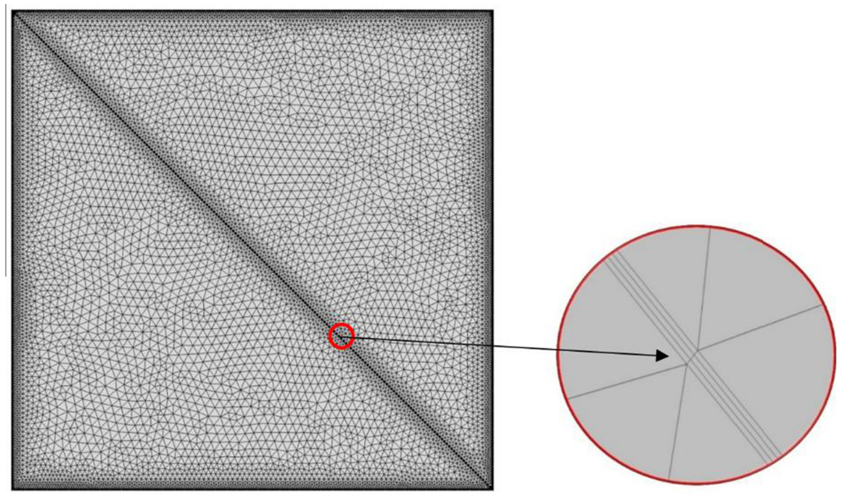

(a) (b)

Fig. 3. The schematic of the utilized grid for Case 3 (a): general view; (b): a close view of the membrane.

Table 3
Comparing reported Nusselt number on hot wall at present study with other for square cavity ($Pr = 0.7$) in various Rayleigh number.

Ra	10^3	10^4	10^5	10^6
Deng and Tang [5]	1.1180	2.2540	4.5570	–
Anandalakshmi and Tanmay [6]	1.1179	2.2482	4.5640	–
Vahl Davis [7]	–	2.2430	4.5190	8.8800
Shi and Khodadahi [8]	–	2.2470	4.5320	8.8930
Sathiyamoorthy and Chamkha [9]	–	2.2530	4.5840	8.9210
Nag et al. [10]	–	2.2400	4.5100	8.8200
Present study	1.1178	2.2450	4.5237	8.8663

Table 4
Comparing the average Nusselt number reported in Kaminski and Prakash [11] and present study when $Pr = 0.7$.

Gr	κ^*	Kaminski and Prakash [11]	Present study
10^3	1	0.87	0.87
	5	1.02	1.02
	10	1.04	1.04
	∞	1.06	1.06
10^5	1	2.08	2.08
	5	3.42	3.40
	10	3.72	3.70
	∞	4.08	4.06
10^6	1	2.87	2.86
	5	5.89	5.85
	10	6.81	6.80
	∞	7.99	7.99
10^7	1	3.53	3.51
	5	9.08	9.02
	10	11.39	11.30
	∞	15.09	15.08

[*] $\kappa = k_s/k_f$.

Table 5
Comparing the valves of $\Delta\psi_{ext}$ reported in Ben-Nakhi and Chamkha [12] and evaluated results in the present study when $Pr = 0.707$, $Ra = 10^5$, $\varepsilon = 105°$ and $L_f = 0.35$.

κ	Ben-Nakhi and Chamkha [12]	Present study
1	11.38	11.30
5	13.10	13.10
10	13.30	13.20
∞	13.34	13.30

[*] $\kappa = k_s/k_f$.

depicted. In Fig. 4, ε is the angle between the fin and the vertical direction, L_f is the dimensionless length of the fin and κ is ratio of the solid to fluid thermal conductivities coefficients (k_s/k_f). In addition, a detailed comparison between the values of the streamlines obtained in the present study, using the finite element method, and the results reported by Ben-Nakhi and Chamkha, obtained using the finite volume method, is shown in Table 5. This table and Fig. 4 show excellent agreement between the results of the present study and the previous study available in the literature.

Kahveci [4] has examined the natural convection heat transfer in a cavity with horizontal adiabatic walls and isothermal sidewalls subject to a temperature difference. The author has considered a solid partition with finite thickness and thermal conductivity inside the cavity, dividing the cavity into two sub cavities. In the study of Kahveci r_w is the dimensionless thickness of the partition, and $r_k = k_f/k_s$ is the ratio of the thermal conductivities of the partition (k_s) and the fluid (k_f). The dimensionless horizontal distance of the center of the partition (x_p^*) from the left wall is denoted by $x_p = x_p^*/L$ In Fig. 5, the local Nusselt number at various Rayleigh numbers reported by Kahveci is compared with the study results of the present study when $r_w = 0.1$, $r_k = 0.01$ and $x_p = 0.5$ on the hot wall according to the vertical distance have been recorded.

As an unsteady case, a comparison between the results of the present study and those reported by Xu et al. [13] is performed in Fig. 6. Xu et al. have considered the problem of the partitioned cavity, studied by Kahveci [4], and developed the problem to the unsteady case. Xu et al. has assumed a very thin and thermal conductive solid partition inside the cavity and hence neglected the effect of conductive heat transfer in the partition.

It is should be noticed that the introduction of the non-dimensional parameters in the study of Xu et al. is different than those utilized in the present study. In the study of Xu et al., the non-dimensional time was introduced as $\tau = t\alpha Ra^{1/2}/H^2$ and $x = x^*/H$. Therefore we have followed the notation and non-dimensional form of the governing equations in the study of Xu

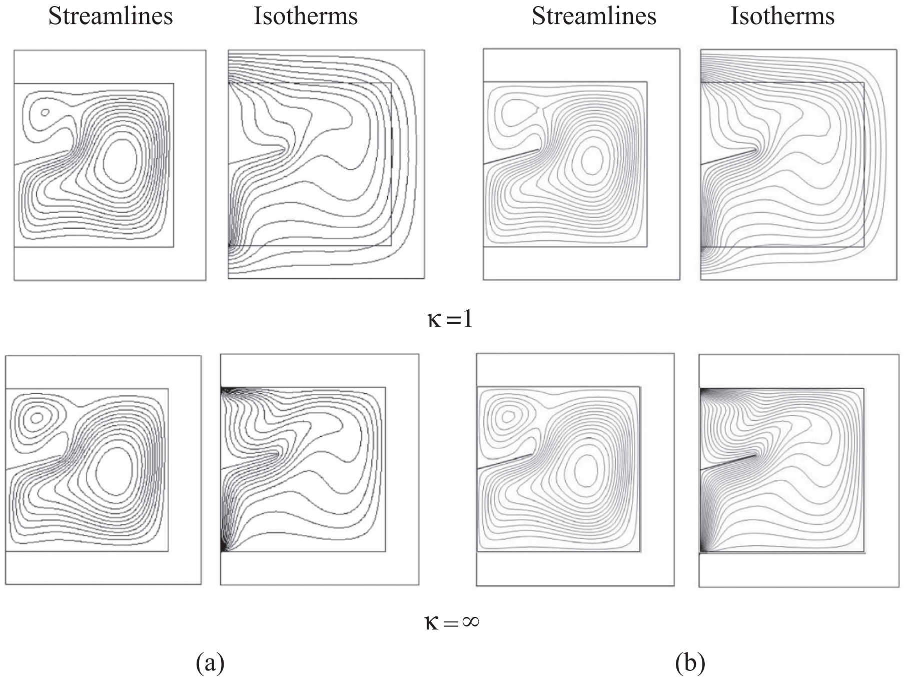

Fig. 4. Comparing contour of isotherm and streamlines when $Pr = 0.707$, $Ra = 10^5$, $\varepsilon = 105°$ and $L_f = 0.35$: (a) Ben-Nakhi and Chamkha [12]; (b) present study.

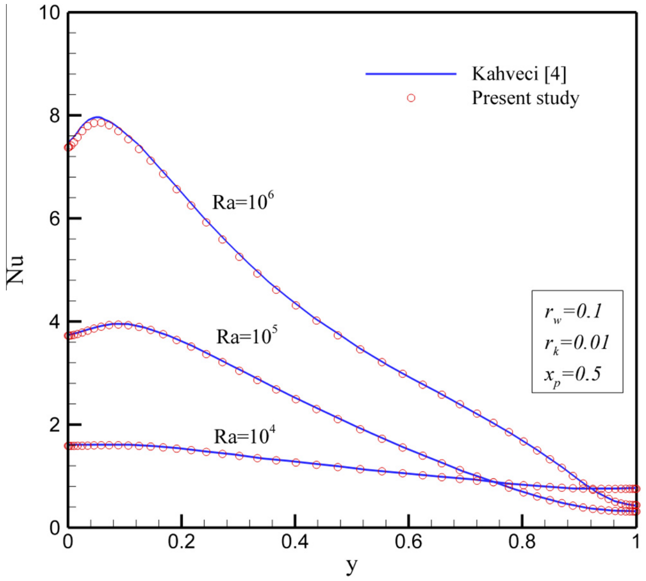

Fig. 5. Comparing value of local Nusselt number along the hot wall for various Rayleigh numbers at $r_w = 0.1$, $r_k = 0.01$ and $x_p = 0.5$ with present study.

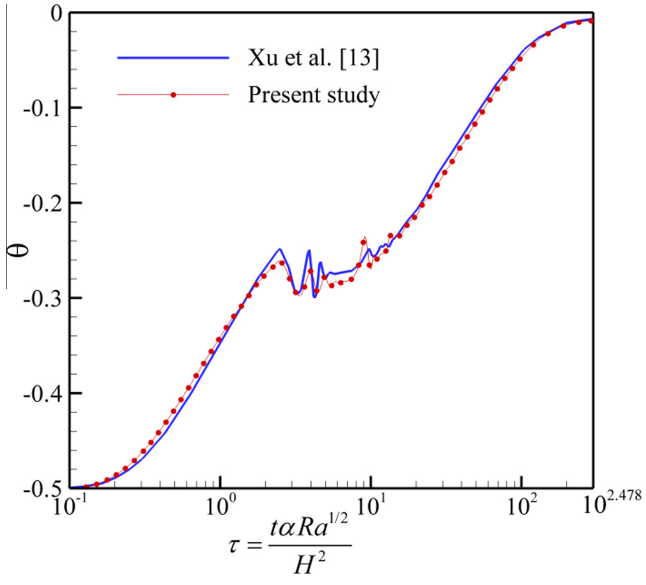

Fig. 6. Comparison of the temperatures histories between the results of present study and the results reported by Xu et al. [13] at the point ($x = 0.0083$, $y = 0.375$) at $Ra = 9.2 \times 10^8$ and $Pr = 6.63$.

et al. for the sake of comparisons. Here, a comparison between the reported temperature history vs. time for a point at the non-dimensional location of (0.0083, 0.375) in the vicinity of the partition is performed. The results for different grid sizes are plotted in Fig. 6. This figure indicates that the time history of the present study and the results of Xu et al. are in very good agreement.

As a comparison with experimental results for the cavity with solid partitions, the experimental results reported by Nishimura et al. [14] have been considered. Nishimura et al. have experimentally examined the natural convection heat transfer in a rectangular cavity divided into sub cavities by multiple partitions. The ratio of height (H) to length of the cavity (L) was four. The top and bottom walls of the cavity was well insulated while the side walls are at constant temperature of T_h and T_c. Nishimura et al. have considered a cavity without a partition ($N = 0$), and cavities containing one ($N = 1$) and two ($N = 2$) rigid partitions. They measured the average Nusselt number at sidewalls and reported the results for different values of Rayleigh numbers. A comparison between the experimental results measured by Nishimura et al. and the numerical results of the present study is reported in Fig. 7. As seen, there is a very good agreement between the numerical and experimental results.

As a final validation, the results of the present study are compared with the results of Küttler and Wall [15] for the case of unsteady flow interaction between the fluid and the flexible solid wall (FSI). Küttler and Wall have considered the lid-driven square cavity with a flexible bottom wall. The size of the cavity is unity (i.e. $L = 1$) and the lid (top wall) is driven by a prescribed periodical velocity of $u_x = (1 - \cos(2\pi t/5))$ m/s. A schematic view of the problem is depicted in Fig. 8. The kinematic viscosity and the density of the fluid was adopted as $\nu = 0.01\text{m}^2/\text{s}$ and $\rho_f = 1.0\ \text{kg/m}^3$. The thickness of the bottom flexible wall was adopted as 0.002 while the Young's modulus and density of the flexible wall was $E = 250\ \text{N/m}^2$ and $\rho_s = 500\ \text{kg/m}^3$. It should be noted that in the study of Küttler and Wall, the possible effect of the buoyancy forces and heat transfer as well as the effect of the weight of the flexible wall were neglected. We have also neglected these effects in the present study for the sake of comparison. In Fig. 9, the shape of the flexible wall after 7.5 s is compared with the results addressed by Küttler and Wall. As seen, there is good agreement between the results of the present study and the results reported by Küttler and Wall.

4. Results and discussion

In order to report the results, the default values of the non-dimensional parameters such as $Ra = 10^7$, $Pr = 6$, $E_\tau = 1.4\text{E}16$ and $F_v = \pm 1.6\text{E}{-2}$ are used otherwise the value of the non-dimensional parameters will be stated. In a real world application, the membrane at the initial condition is bended due to its own weight. However, in the present study, in order to allow for possible comparisons with problems using fixed membranes, the initial state of the membrane is assumed to be a straight line. Although this assumption can affect the initial state of the solution, it does not, however, significantly affect the final solution and the steady shape of the membrane.

Figs. 10 and 11 depict the velocity and temperature contours for the time spans. In Fig. 10, the non-dimensional velocities are divided by 100 then plotted for convenience. Therefore, the non-dimensional velocities of Fig. 10 are scaled to 100. As seen, at first, the partition is a straight line at rest. Starting the heat transfer from the hot side to cold side induces a natural convection flow and heat transfer due to buoyancy forces resulting in displacement of the membrane and consequently, the grids inside the cavity. At the early stages, the flow starts from the regions next to the membrane where the temperature differences and the buoyancy forces are strong, while the other regions are almost unaffected. Thus, in this stage, the membrane is under the direct influence of the flow patterns at the right and left regions next to the membrane. In this situation, the shape of the membrane is in agreement with the nature of the circulation of the fluid in the cavity and different stages of the flow transitions. The different stages of flow transitions for a partitioned cavity have been reported by Xu et al. [13] and a time history of temperature variation was depicted in Fig. 6. However, it should be noted that the shape of the membrane in the present study is not only under the influence of the flow patterns but also its elastic nature. Hence, it goes through continuous changes to ultimately reach a final shape. In this case (i.e. the steady state shape), the membrane is positioned toward the cold region. This is due to the position of the open boundary of II in the hot region, which is placed next to the membrane. Attention to the position of

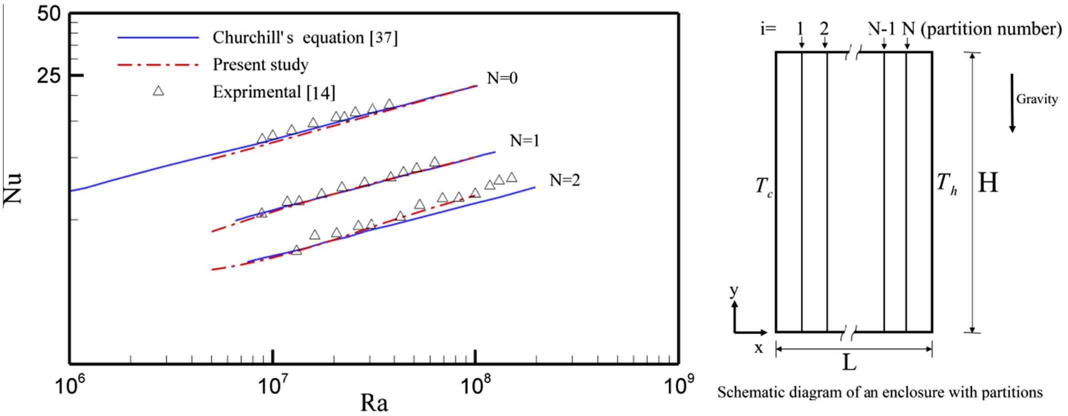

Fig. 7. Comparing the average Nusselt number evaluated in the present study and the experimental results reported by Nishimura et al. [14] and the Churchill's relation [37] for a rectangular enclosure with various of partitions (N) as a function of Rayleigh number when $H/L = 4$ and $Pr = 6$.

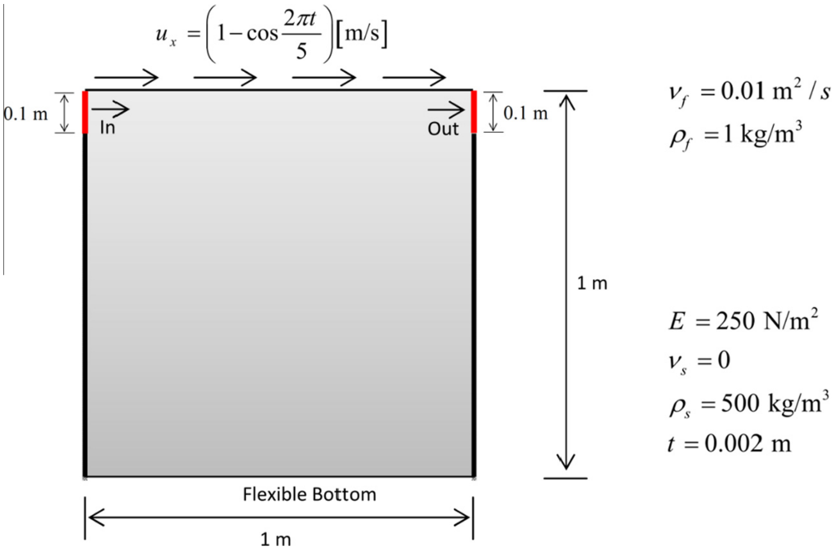

Fig. 8. Driven cavity with flexible bottom (Küttler and Wall [15]).

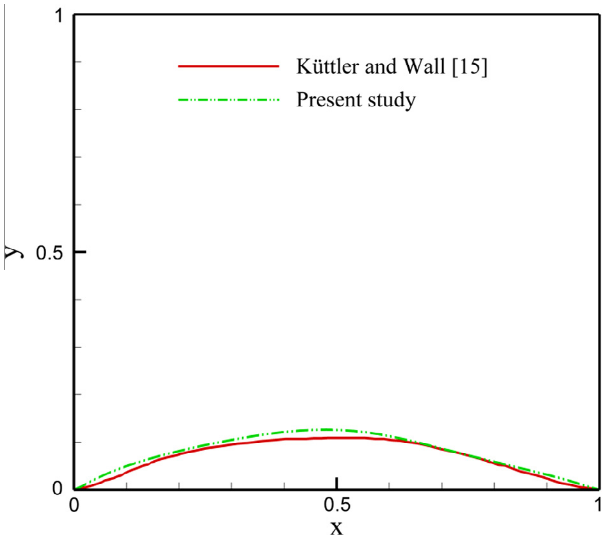

Fig. 9. The shape of the flexible wall after 7.5 s is compared with the results addressed by Küttler and Wall [15].

the open boundaries next to the top regions of the cavity shows that at the hot region, the zero pressure area, the open boundary, is placed at the end of the hot boundary layer next to the hot wall. This is where the hot jet formed from the bottom of the cavity next to the hot wall reaches the top of the cavity. In contrast, the open boundary at the cold side is placed at the beginning of the cold boundary layer, where the cold fluid next to the cold wall starts to get cold and moves downward. Therefore, the flow and pressure patterns in the cavity are indeed not symmetric.

Fig. 10 shows that the velocity is zero at the beginning and then the flow gets stronger and stronger. At the time step of $\tau = 10^{-3}$, next to the open boundaries, various levels of velocity contours can be observed, which indicate the velocity gradient of the fluid in the vicinity of these boundaries. The entrance or ventilation of fluid from the open boundaries induces a secondary flow in the domain. However, this secondary flow is very weak as the size of the open boundaries is very small. When the partition tends to move upward, the flow tends to enter the cavity at the hot side in a direction opposed to the circulation of the flow circulation. At the same time, a similar situation is held true at the cold side where the membrane tends to reduce the volume of the cold region and the flow tends to exit from the corresponding open

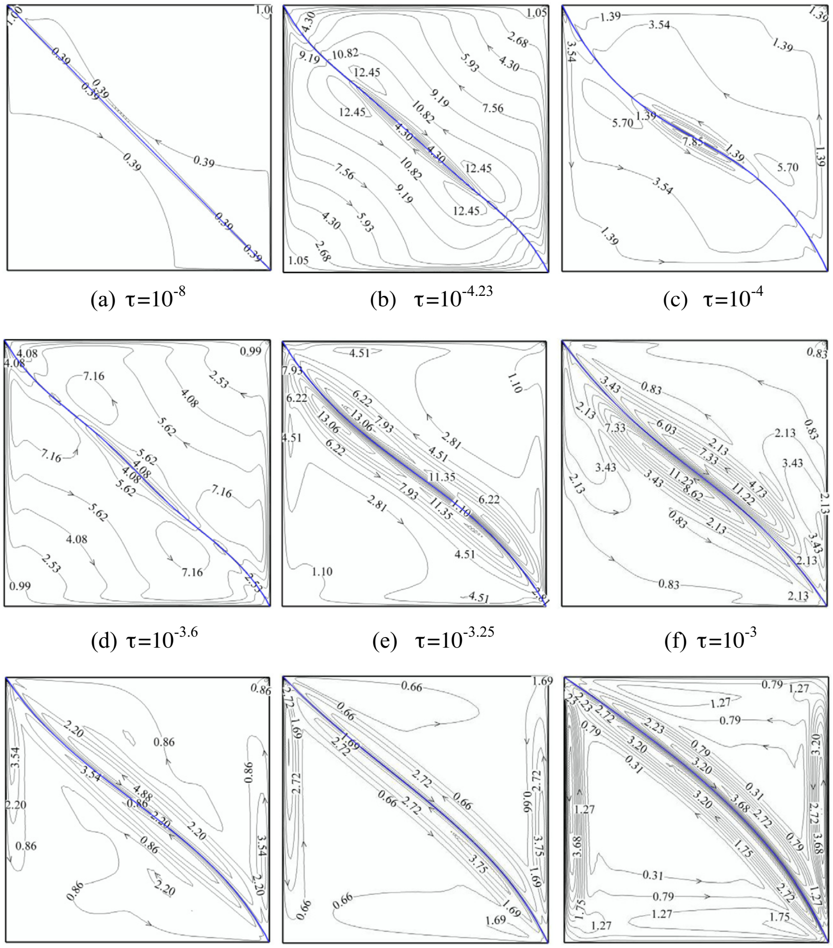

(a) $\tau=10^{-8}$ (b) $\tau=10^{-4.23}$ (c) $\tau=10^{-4}$

(d) $\tau=10^{-3.6}$ (e) $\tau=10^{-3.25}$ (f) $\tau=10^{-3}$

(i) $\tau=10^{-2.5}$ (j) $\tau=10^{-2}$ (k) $\tau=10^{-1}$

Fig. 10. Counter of fluid velocity at various dimensionless times for $E_\tau = 10^{14}$, $F_v = 0$, $Ra = 10^7$ and $Pr = 6$; (the velocities are scaled to 100).

boundary. In this situation, the induced secondary flow would be in a direction opposed to the direction of the flow circulation.

In this case, the membrane starts to move upward and form its final shape. At the final stages when the flow reaches the steady state situation, two distinct counter-clock wise flows in the cavity are obvious.

Fig. 11 shows that at the beginning there are two distinct hot and cold regions inside the cavity. As time starts elapsing, the heat transfer commences very close to the membrane. In this region, the dominant mechanism of heat transfer is diffusion as there is no slip flow at the surface of the membrane. Then, the flow velocity starts getting stronger and consequently the advection mechanism inside the cavity gets stronger. In this situation, most parts of the cavity have seen the effect of heat transfer. In addition, at the time step of $\tau = 10^{-5}$, the entrance of fresh hot fluid at the open boundary is commencing to develop. Next to the open boundaries various levels of velocity contours can be observed, which indicates the velocity gradient of the fluid in the vicinity of these boundaries. As the membrane continues its transient oscillatory movements, the entrance or ventilation of flow from open boundaries also induces a secondary flow and heat distribution inside the cavity.

The results of the dimensionless maximum stress corresponding to time steps of Fig. 10 have been reported in Table 6. It is interesting to observe that at the early stages of the commencement of natural convection heat transfer, the membrane goes through its highest maximum stress, then the maximum stress of the membrane reduces for a while and finally rises again until the membrane reaches its steady state condition. At the steady state condition, the maximum observed stress is $\sigma = 3.89 \times 10^{12}$ while at the time step of $\tau = 10^{-4}$, it is about $\sigma = 4.89 \times 10^{12}$.

Fig. 12 shows the final form (steady form) of the membrane for three cases of: (I): the density of membrane is lower than the density of the fluid ($F_v = 1.64 \times 10^{-2}$), (II): the density of the membrane is about the density of the fluid ($F_v = 0$) and (III): the density of membrane is higher than the density of the fluid ($F_v = -1.64 \times 10^{-2}$).The initial state of the partition is also depicted for the sake of a simple comparison. As seen, the heavy membrane deflects downward while the light membrane moves upward. The membrane with the density about the density of the fluid (negligible buoyancy and gravity forces) moves slightly upward. As mentioned, this is due to the effect of the open boundaries on the distribution of the flow and pressure gradient in the cavity. In the hot triangular sub cavity, the hot fluid moves upward along the vertical wall until it reaches to the open boundary, and then interacts with the membrane and gets cooler, resulting in the flow of the fluid along the membrane. In the cold sub-cavity, the cold fluid tends to move downward along the vertical cold wall until it reaches to the membrane and gets warmer and starts moving upward along the membrane. As both of the open boundaries are placed close to the top of the cavity, the system of flow and pressure distribution in the cavity is not symmetric, and consequently, the membrane moves upward due to close interaction with the

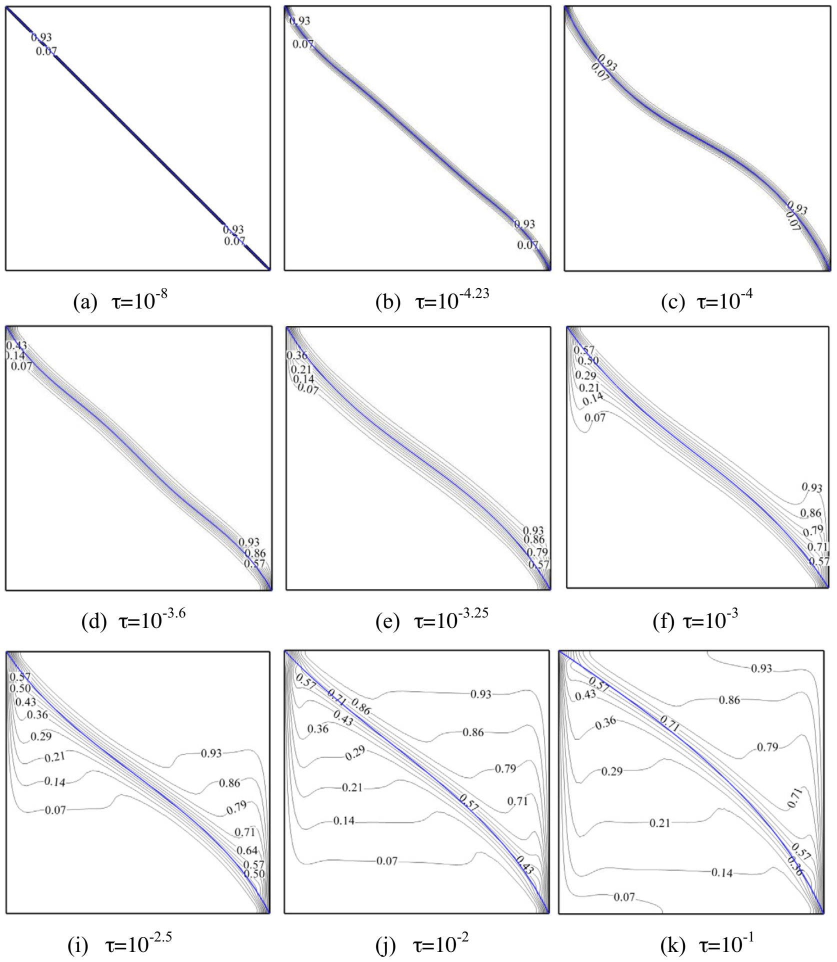

(a) τ=10^{-8} (b) τ=10$^{-4.23}$ (c) τ=10^{-4}

(d) τ=10$^{-3.6}$ (e) τ=10$^{-3.25}$ (f) τ=10^{-3}

(i) τ=10$^{-2.5}$ (j) τ=10^{-2} (k) τ=10^{-1}

Fig. 11. Counter of temperature at various dimensionless times for $E_\tau = 10^{14}$, $F_v = 0$, $Ra = 10^7$, and $Pr = 6$.

Table 6
The maximum dimensionless von Mises stress (σ) in membrane during the dimensionless time (τ).

τ	σ (von Mises stress) $\times 10^{12}$
10^{-8}	0.00774
$10^{-4.23}$	2.11
10^{-4}	4.89
$10^{-3.6}$	1.83
$10^{-3.25}$	1.39
10^{-3}	1.37
$10^{-2.5}$	2.14
10^{-2}	2.49
10^{-1}	3.89

open boundary in the hot sub-cavity and the counter-clock wise circulation of the flow.

The problem has been also solved for a cavity with constant pressure point constraints of relative pressure of zero instead of open boundaries. When the natural convection flow reaches its steady state solution, it is expected that the error of the constant pressure point assumption converges to zero. This is because of the fact that the membrane is still, and hence, there is no change in the volume of the partition. Thus, both of the mass balance and the constant point pressure constraint could be hold true in this situation, the same as an enclosure with a solid partition. The following figure compares the results of these two models at the steady state solution. In Fig. 13, the steady state shape of the membrane is plotted for two cases of the cavity with open boundaries and cavity with pressure point constraints when the body force of F_v is zero. As seen, in the case of cavity with a pressure point constraint the shape of the membrane is symmetric respect to the center of the cavity.

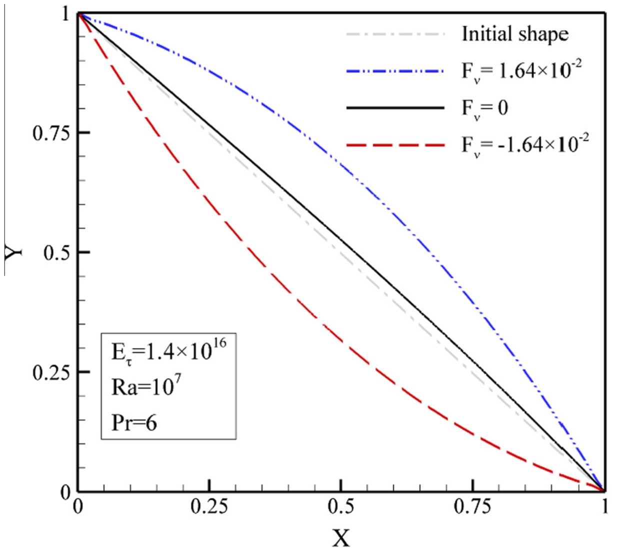

Fig. 12. Effect of buoyancy parameter (F_v) on the steady state shape of the membrane at $E_\tau = 1.4 \times 10^{16}$, $Ra = 10^7$and $Pr = 6$.

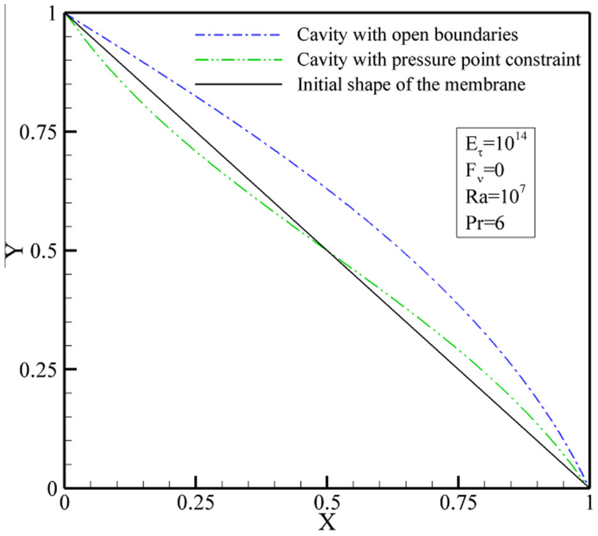

Fig. 13. Steady state shape of the membrane with\without open boundaries when $E_\tau = 10^{14}$, $F_\upsilon = 0$, $Ra = 10^7$and $Pr = 6$.

Fig. 14(a)–(c) illustrates the corresponding steady streamlines and isotherms of the membranes depicted in Fig. 12. As seen, the weight parameter of the membrane is the dominant effect for the final shape of the membrane. When the weight of the membrane is equal to the buoyancy forces acting from the fluid to the membrane (i.e. the density of the membrane and the fluid are equal), the membrane tends to move upward due to the velocity and pressure distributions inside the cavity as discussed earlier. The positive weight parameter indicates that the density of the membrane is lower than the density of the fluid and hence, again the membrane would move further upward. In contrast, the negative value of the weight parameter indicates that the density of the membrane is higher than the density of the fluid, and hence, the membrane moves downward against the nature of the interaction between the solid and fluid structure. The streamlines in all figures confirm the circulation of the fluid inside the cavity. The streamlines are close together in the vicinity of the membrane and walls indicating that the velocity gradients are high at these regions. Ultimately, it is clear that there is no streamline going through the open boundaries which shows zero mass transfer from the open boundaries. This is in very good agreement with the physics of the incompressible fluid flow as there is only one open cavity at each enclosure and the membrane is quiescent.

Similar to the streamlines, the isotherms are very close together next to the membrane which shows high temperature gradient and heat transfer rate at this region. However, in contrast with the streamlines, the isotherms are only close together near the top left and bottom right corners of the cavity. From the isotherms, it is clear that all of the membrane is almost isothermal with a non-dimensional temperature of about 0.5, i.e. a temperature about mean temperature of the hot and cold walls, and only few isotherms cross the membrane near the corners. However, when the partition moves upward, its temperature smoothly rises and when it moves downward its temperature decreases and tends to the temperature of the cold regions in the bottom cold enclosure.

Fig. 15(a)–(d) illustrates the isotherms and streamlines for various values of the Rayleigh number for the steady-state solution when the density of the partition is about the density of the fluid $F_v = 0$. The streamlines for low values of the Rayleigh number, i.e. $Ra = 10^4$ and $Ra = 10^5$, are almost uniform and confirm a smooth flow circulation in the cavity. In these cases, the flow is very weak and consequently, the pressure distributions are weak and hence, the membrane is almost a straight line. For the case of $Ra = 10^4$, the isotherms show almost a liner distribution in the cavity which indicates that the diffusion heat transfer is the dominant mechanism of heat transfer. As the Rayleigh number increases, the advection mechanism also gets important and as a result, for $Ra = 10^5$ the isotherms start to smoothly follow the streamlines patterns in the cavity. For higher values of the Rayleigh number this effect increases. For a very high value of the Rayleigh number ($Ra = 10^7$) the isotherms completely follow the streamlines. It is also clear that the increase of the Rayleigh number increases the strength of the fluid–solid interaction forces, which results in the increase of the membrane deflection.

In Fig. 16(a) and (b), the effect of the non-dimensional elastic modulus on the shape of the membrane for maximum displacement and steady-state situations is illustrated. The case of membrane maximum displacement is considered a case in which a point of the membrane goes through maximum displacement from its initial position among all of the time steps. Indeed, the case of maximum displacement is a global case corresponding to the maximum displacement of the membrane among all of the movements of the membrane. For example, in the case of $E_\tau = 10^{15}$ the maximum displacement of the membrane occurs at $\tau = 10^{-4.17}$. From the shape of the membrane, it is also clear that the place of maximum deflection of the membrane is at the ¼ length from the corners.

Fig. 17 depicts the dimensionless time history of the discharges or intake of fluid through the open boundaries. In Fig. 17, the dimensionless flow rates for the boundaries of left and right are compared from the beginning of heat transfer, i.e. $\tau = 0$, until the steady-state condition, i.e. $\tau = 0.1$. The dimensionless flow rate is calculated as $Q = \int_L udL$. At the left wall, the flow enters and exits from the right wall. Here, both flow rates are plotted as positive for the sake of comparison. As seen, the inlet and outlet flow rates are coincident which confirms the incompressibility of the flow and mass conservation in the ALE system and the cavity. As the natural convection gets stronger and the membrane moves upward monastically, after a while the deflection of the membrane grows, and then, the elastic effect of the membrane gets stronger and the flow transients occur. This is where the membrane goes through some sine-wave-like deflections and finally reaches its final steady shape. At the steady-state situation, the shape of the membrane remains constant, and hence, the flow rates are zero.

Fig. 18 shows the dimensionless temperature history for point *A* located at the coordinates of (0.25, 0.75) in both material (fixed with the geometry) and spatial (moving with the grid) coordinate systems. The material coordinate system is fixed with the coordinate of the geometry and does not go through any displacement. In contrast, the spatial coordinate system is based on the grid points and goes through movements with the motion of the grid. Hence, it can be said that the spatial coordinate in Fig. 18 is a material point on the flexible membrane. Indeed, the results of the temperature history for point *A* in the material coordinate system shows the temperature of point *A* as fixed in the space (point *A* will always be motionless. Therefore, for point *A* in the material coordinate system, the membrane could be above of this point or below it during time, as the membrane is in motion). The temperature history for point *A* in the spatial coordinate system shows the temperature of the point *A* if it moves with the grid. Hence, the membrane will never cross this point in the spatial coordinate system as it always moves with the grids associated with the motion of the membrane. Fig. 18 shows that the temperature of point *A* in material coordinate system goes through sudden temperature variations as the boundary layer associated with the membrane repeatedly crosses this point. In contrast, the temperature history of point *A* shows a smooth temperature variation as it moves with in the boundary layer of the temperature in the vicinity of the

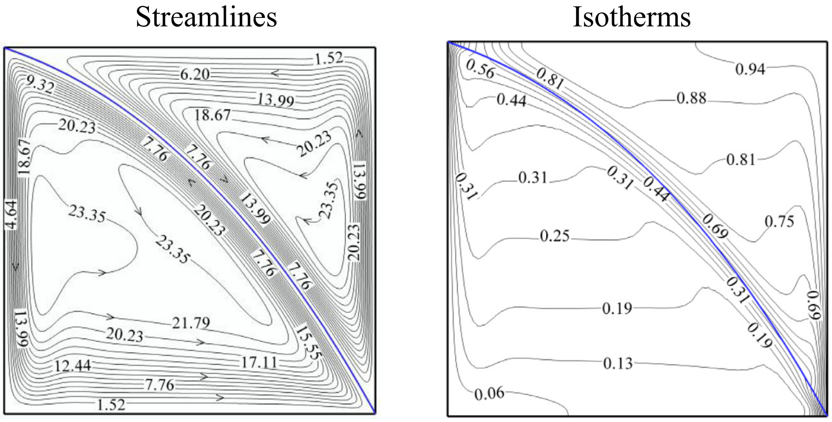

(a) F_v=1.6×10^{-2}

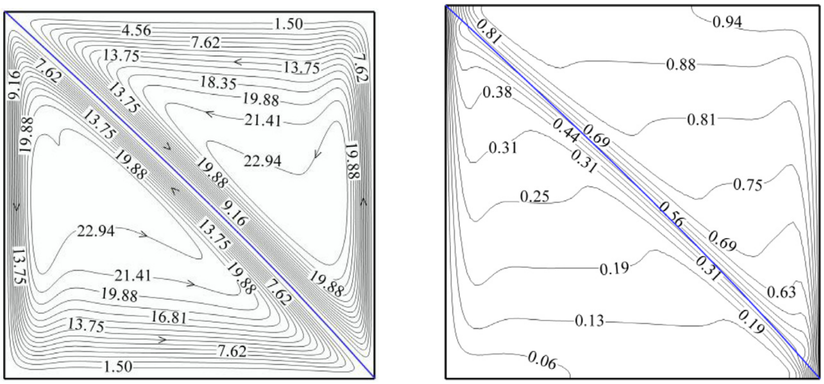

(b) F_v=0

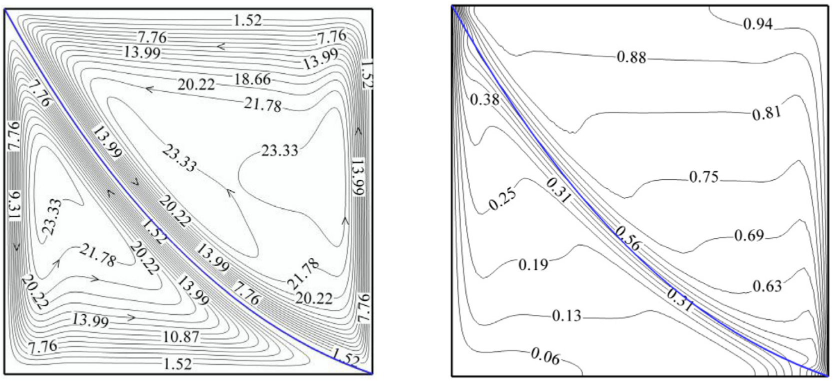

(c) F_v=-1.6×10^{-2}

Fig. 14. Isothermal and streamlines of the steady state solution for various weight parameter of the membrane (F_v) when $Ra = 10^7$, $Pr = 6$ and $E_\tau = 1.4 \times 10^{16}$.

membrane. Indeed, this point shows the variation of temperature of a sensor attached next to the membrane which moves with the membrane.

Fig. 19 shows the maximum non-dimensional stress in the membrane as a function of the modulus of elasticity and the Rayleigh number. Starting from the initial condition and by elapsing of time, the membrane goes through different deflections until it reaches a steady state situation and gets still. Considering the time history of the membrane, the maximum stress is the maximum observed stress in time history of the membrane deflection. The maximum stress may not necessarily occur at the steady state condition. The maximum deflection, is the maximum displacement of the membrane from its original (initial) position.

Fig. 19(a) interestingly shows that the increase of the non-dimensional modulus increases the non-dimensional tension in the membrane. Indeed, as the membrane gets stiffer, it becomes more resistant to the fluid force and results in higher values of tensions. Fig. 19(b) also indicates that the increase of the Rayleigh number increases the induced maximum tension in the membrane. Indeed, the increase of the Rayleigh number increases the motion of the fluid and consequently, boosts the fluid-structure interactions.

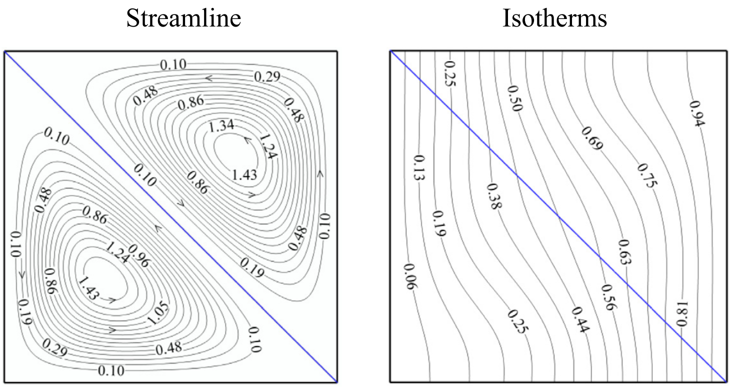

(a) $Ra=10^4$

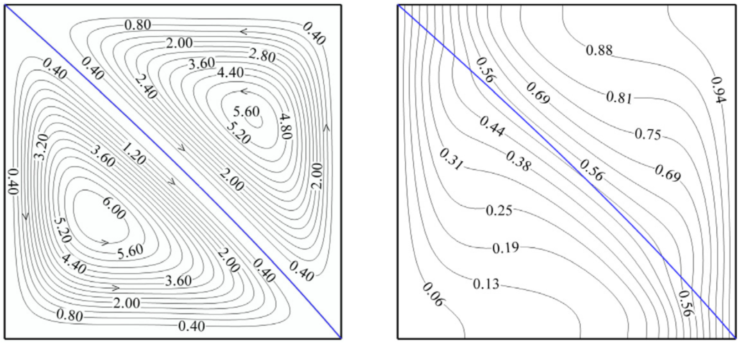

(b) $Ra=10^5$

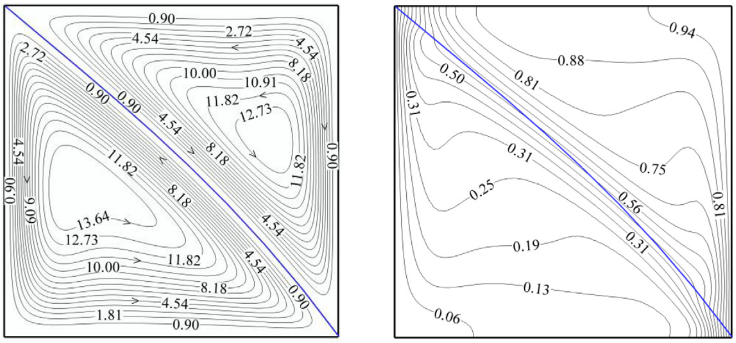

(c) $Ra=10^6$

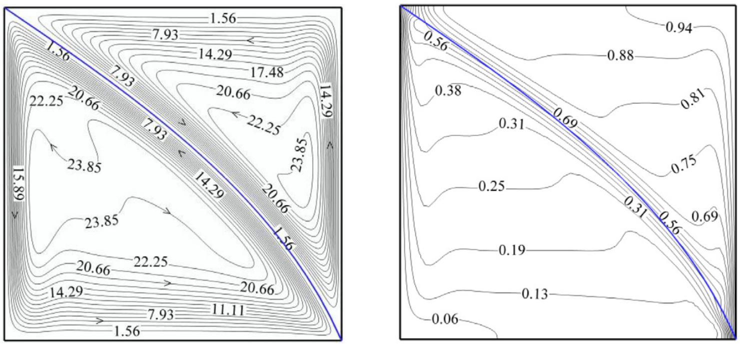

(d) $Ra=10^7$

Fig. 15. The isotherms and streamlines at for steady state for $Pr = 6.0$, $E_\tau = 10^{14}$ and $F_v = 0$.

Fig. 20 depicts the local heat transfer on the hot and cold walls for various time steps. Fig. 20 shows the maximum local Nusselt number at the hot wall occurs next to the bottom part of the hot wall (i.e. $y = 0$) where the cold fluid starts to reach the hot wall. In contrast, the maximum local Nusselt number occurs close to the top part of the cold wall (i.e. $y = 1$) where the hot fluid reaches the wall. The behavior of the local Nusselt number at both walls is almost the same. However, the maximum Nusselt number at

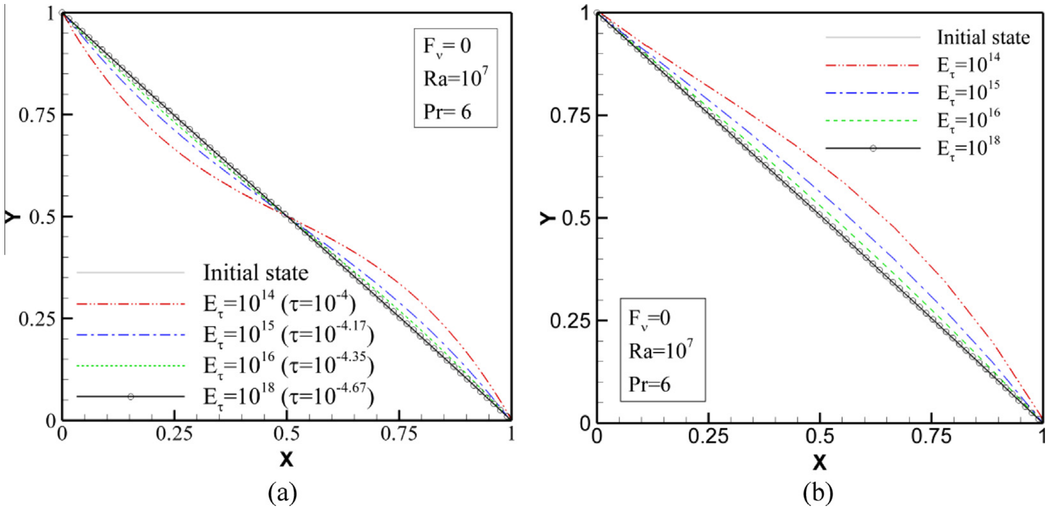

Fig. 16. The effect of elastic modulus on the shape of the membrane when $Ra = 10^7$ and $Pr = 6$ and $F_v = 0$; (a): maximum displacement (b) steady state.

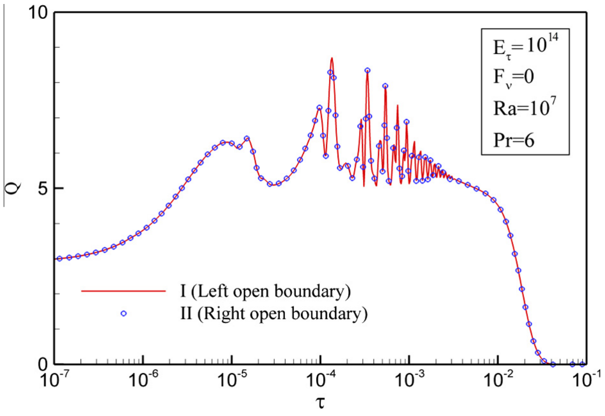

Fig. 17. Compare the discharge passing through the open boundaries at $E_\tau = 10^{14}$, $F_v = 0$, $Ra = 10^7$ and $Pr = 6$.

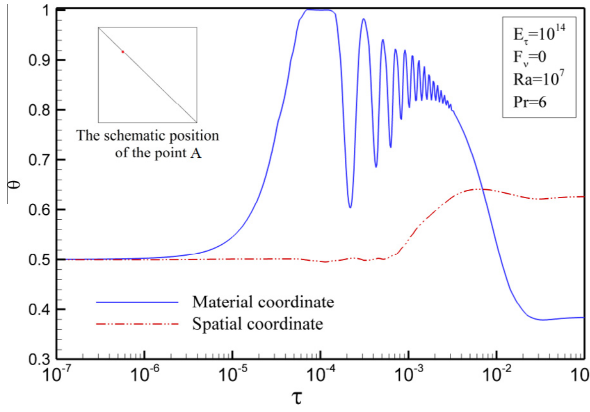

Fig. 18. Comparing time series of temperature in both material and spatial coordinates for the point (0.25, 0.75) at $E_\tau = 10^{14}$, $F_v = 0$, $Ra = 10^7$ and $Pr = 6$.

$\tau = 10^{-2}$ for the cold wall is higher than that of the hot wall. This is because of the upward motion of the membrane, which smoothly reduces the size of the cold enclosure and reduces the distance between the membrane and the cold wall. Indeed, the motion of the membrane toward the cold enclosure deteriorates the symmetry of the cavity, flow and heat transfer, and hence, the behavior of the local Nusselt number at the right and left walls is not exactly symmetric.

Fig. 21 shows the average Nusselt number at the hot wall as a function of non-dimensional time for various values of the Rayleigh number for two cases of flexible membrane and rigid partition $F_v = 0$ and $Pr = 6$. As seen in both cases, at the early stages of the heat transfer, the average Nusselt number at the hot wall is low. There are slight differences between the magnitude of the reduced Nusselt number ($NuRa^{-1/4}$) for the cases of $Ra = 10^7$ and $Ra = 10^5$ at $\tau = 10^{-8}$. This is because of the fact that the temperature in the hot enclosure next to the hot wall is uniform and equals to the temperature of the hot wall at the beginning of heat transfer and the dominant regime of heat transfer is conduction. The observed difference is because of the difference in magnitude of Rayleigh number. After a while, the fluid next to the membrane gets colder as a result of the interaction with the cold fluid in the cold enclosure through the thermal conductive membrane. The cold fluid due to diffusive and advective heat transfer mechanisms tends to change the temperature distribution in the hot enclosure. As the temperature gradient develops in the enclosure, the buoyancy force boosts and the advective heat transfer mechanism gets stronger. Finally, the stream of cold fluid starts form the membrane and reaches to the hot wall. The cold fluid starts to remove heat from the hot wall and gets hot again. In this process and as the velocity of the fluid inside the enclosure boosts, the average Nusselt number at the hot wall increases. There are some local peaks for the average Nusselt number which are the result of the transient stages, which were discussed in the temperature time series in Fig. 6 and in details by Xu et al. [13]. After elapsing a long time, the fluid and heat transfer reach to a steady situation and then the heat transfer from the hot wall and the Nusselt number reaches to its constant steady value. This figure also shows that the increase of the Rayleigh number increases the average Nusselt number. Following the study of Xu et al. [13], the steady state time scale for the case of a cavity divided by a rigid partition can be evaluated as: $\tau_f \sim 0.5 \times Ra^{-1/4}$ which gives $\tau_f = 0.028$ for the case of $Ra = 10^5$ and $\tau_f = 0.009$ for the case of $Ra = 10^7$. The trend and the order of magnitude of the steady state time scale of the partitioned cavity are in good agreement with the results of Fig. 21. A comparison between the results of the flexible membrane and the rigid partition shows that the presence of a flexible membrane could results in the increase of τ_f (the required non-dimensional steady state time) when the Rayleigh number is high, i.e. $Ra = 10^7$. The presence of a flexible membrane can also decrease τ_f when the Rayleigh

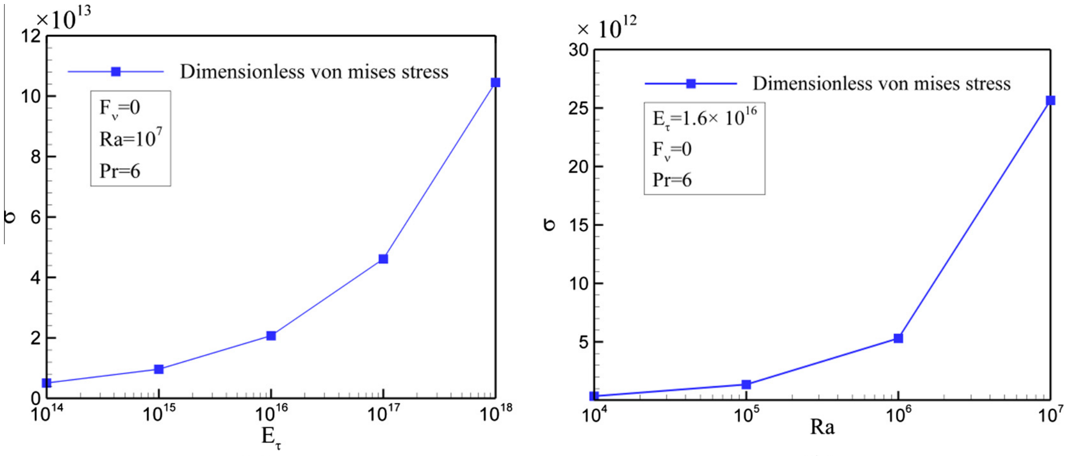

(a) (b)

Fig. 19. The stress in the membrane (a) as a function of elastic modulus when $F_\upsilon = 0$, $Ra = 10^7$ and $Pr = 6$; (b) as a function of Rayleigh number when $E_\tau = 1.4 \times 10^{16}$, $F_\upsilon = 0$ and $Pr = 6$.

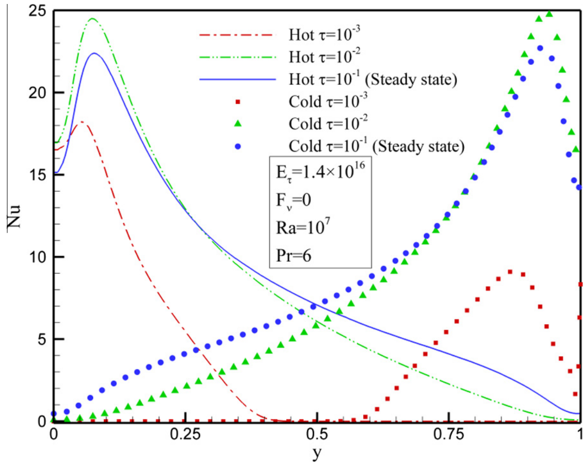

Fig. 20. The local heat transfer on the hot wall (a) and cold wall (b) reported by height of cavity when $E_\tau = 1.4 \times 10^{16}$, $F_\nu = 0$, $Ra = 10^7$ and $Pr = 6$.

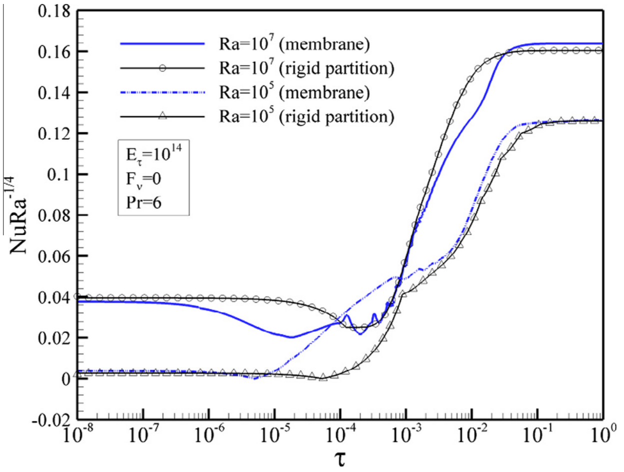

Fig. 21. The average Nusselt number over dimensionless time for hot wall $F_\nu = 0$ and $Pr = 6$; $E_\tau = 10^{14}$ in the case of flexible membrane.

Table 7
The Nusselt numbers and the streamline on the wall hot at various Rayleigh numbers ($Pr = 6$ and $E_\tau = 1.4 \times 10^{16}$).

	Ra		10^4	10^5	10^6	10^7
Cavity with a partition	Rigid partition	$\Delta\psi$	1.1489	6.0235	14.049	24.442
		Nu	1.1827	2.3189	4.6931	9.0217
	Flexible partition	$\Delta\psi$	1.1541	6.3971	15.546	25.460
		Nu	1.1828	2.3489	4.7457	9.2619
Closed cavity	Without partition	$\Delta\psi$	5.1734	11.063	19.827	35.755
		Nu	2.2556	4.5237	8.8663	17.6989

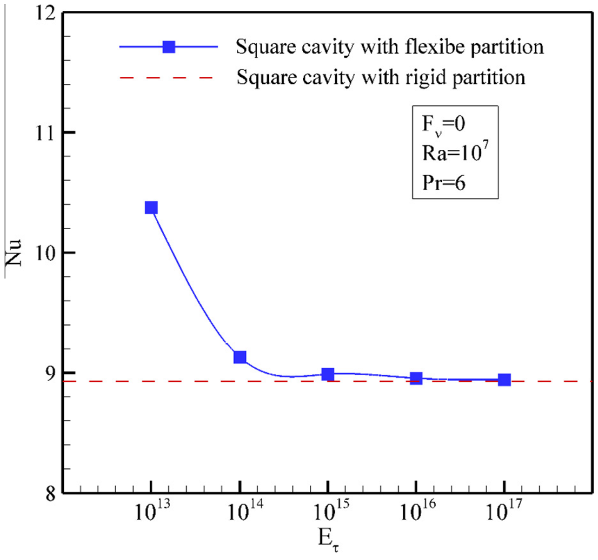

Fig. 22. The average Nusselt number of the hot wall as a function of non-dimensional partition module $E\tau$ in the steady state condition.

number is low, i.e. $Ra = 10^5$. When the Rayleigh number is small, the strength of motion of the fluid is low and the motion of the membrane, releasing from the initial condition, can enhance the flow movement, and hence, the required steady state time decreases. In contrast, when the Rayleigh number is high, the fluid motion is strong, and consequently, the membrane goes through various movements. Hence, it requires more time to reach a steady state condition. Thus, the required steady state time for high values of the Rayleigh number could be higher than that of a rigid partition.

A comparison between the average Nusselt number at the hot wall (*Nu*) and the streamline difference ($\Delta\psi$) corresponding to a cavity with fixed and flexible membrane is shown in Table 7 for various values of the Rayleigh number at the steady-state solution. In Table 7, $\Delta\psi$ is defined as $\psi_{max} - \psi_{min}$ where the subscripts max and min indicate the maximum and minimum values of the streamline function in the cavity, respectively. In the case of simple cavity, the results are reported for a cavity with the pressure point constraint. As seen, when the membrane is flexible, the heat transfer and flow strength are smoothly higher.

Fig. 22 shows the effect of the partition elasticity on the steady state average Nusselt number of the cavity at the hot wall. As seen, when the membrane is very flexible, i.e. $E\tau \sim 10^{13}$, a significant enhancement in the average Nusselt number can be seen. This is due to the fact that for a very flexible membrane, the fluid structure interaction can effectively change the shape of the membrane in a way in agreement to flow patterns. However, as the rigidity of the membrane increases, the average Nusselt number tends to converge to the corresponding average Nusselt number of the rigid partition.

5. Conclusion

The natural convective heat transfer in a partitioned cavity, divided to two sub-cavities by a flexible membrane, was successfully modeled using ALE formulation. The interaction between the fluid and membrane was taken into account using the balance of forces and the continuity of fluid and solid at the interface of the membrane. The effects of the weight of the membrane and the buoyancy forces acting on the membrane were also taken into account. The governing system of equations was formulated and solved using the finite-element method. Different aspects of the governing equations were validated against several benchmark studies available in the literature and found in very good agreement. It was found that the effects of the weight of the membrane and the buoyancy forces, i.e. F_v, on the final shape of the membrane are very important and cannot be neglected. The interaction of the fluid and membrane would change the shape of membrane. The change in the shape of the membrane would consequently affect the heat transfer. It was also found that the heat transfer with a flexible membrane is smoothly higher that of a rigid membrane.

As mentioned, the initial state of the membrane is assumed to be a straight line in the present study. In future studies, the membrane can be released to freely bend, then, the convection heat transfer can be commenced. In addition, in the present study, the membrane was assumed to be highly thermally conductive; however, the finite thermal conductivity of the membrane could also affect the convective heat transfer in the cavity. This situation could be the subject of future studies.

Acknowledgments

The first and second authors acknowledge the financial support of Dezful Branch, Islamic Azad University, Dezful, Iran. The authors acknowledge the Sheikh Bahaei National High Performance Computing Center (SBNHPCC) for providing computational resources. SBNHPCC is supported by scientific and technological department of presidential office and Isfahan University Of Technology (IUT).

References

[1] R. Nasrin, M.A. Alim, A.J. Chamkha, Effects of physical parameters on natural convection in a solar collector filled with nanofluid, Heat Transfer—Asian Res. 42 (1) (2013) 73–88.

[2] A. Baïri, E. Zarco-Pernia, J.M.G. De María, A review on natural convection in enclosures for engineering applications. The particular case of the parallelogrammic diode cavity, Appl. Therm. Eng. 63 (1) (2014) 304–322.

[3] S.C. Kaushik, R. Kumar, H.P. Garg, J. Prakash, Transient analysis of a triangular built-in-storage solar water heater under winter conditions, Heat Recovery Syst. CHP 14 (4) (1994) 337–341.

[4] K. Kahveci, Numerical simulation of natural convection in a partitioned enclosure using PDQ method, Int. J. Numer. Meth. Heat Fluid Flow 17 (4) (2007) 439–456.

[5] Q.H. Deng, G.F. Tang, Numerical visualization of mass and heat transport for conjugate natural convection/heat conduction by streamline and heatline, Int. J. Heat Mass Transfer 45 (11) (2002) 2373–2385.

[6] R. Anandalakshmi, T. Basak, Heat flow visualization for natural convection in rhombic enclosures due to isothermal and non-isothermal heating at the bottom wall, Int. J. Heat Mass Transfer 55 (4) (2012) 1325–1342.

[7] G. de Vahl Davis, Natural convection of air in a square cavity: a bench mark numerical solution, Int. J. Numer. Meth. Fluids 3 (3) (1983) 249–264.

[8] X. Shi, J.M. Khodadadi, Laminar natural convection heat transfer in a differentially heated square cavity due to a thin fin on the hot wall, J. Heat Transfer 125 (4) (2003) 624–634.

[9] M. Sathiyamoorthy, J.A. Chamkha, Analysis of natural convection in a square cavity with a thin partition for linearly heated side walls, Int. J. Numer. Meth. Heat Fluid Flow 24 (5) (2014) 1057–1072.

[10] A. Nag, A. Sarkar, V.M.K. Sastri, Natural convection in a differentially heated square cavity with a horizontal partition plate on the hot wall, Comput. Meth. Appl. Mech. Eng. 110 (1) (1993) 143–156.

[11] D.A. Kaminski, C. Prakash, Conjugate natural convection in a square enclosure: effect of conduction in one of the vertical walls, Int. J. Heat Mass Transfer 29 (12) (1986) 1979–1988.

[12] A. Ben-Nakhi, A.J. Chamkha, Conjugate natural convection in a square enclosure with inclined thin fin of arbitrary length, Int. J. Therm. Sci. 46 (5) (2007) 467–478.

[13] F. Xu, J.C. Patterson, C. Lei, Heat transfer through coupled thermal boundary layers induced by a suddenly generated temperature difference, Int. J. Heat Mass Transfer 52 (21) (2009) 4966–4975.

[14] T. Nishimura, M. Shiraishi, F. Nagasawa, Y. Kawamura, Natural convection heat transfer in enclosures with multiple vertical partitions, Int. J. Heat Mass Transfer 31 (8) (1988) 1679–1686.

[15] U. Küttler, W.A. Wall, Fixed-point fluid–structure interaction solvers with dynamic relaxation, Comput. Mech. 43 (1) (2008) 61–72.

[16] A.J. Chamkha, M.A. Ismael, Conjugate heat transfer in a porous cavity filled with nanofluids and heated by a triangular thick wall, Int. J. Therm. Sci. 67 (2013) 135–151.

[17] S. Parvin, A.J. Chamkha, An analysis on free convection flow, heat transfer and entropy generation in an odd-shaped cavity filled with nanofluid, Int. Commun. Heat Mass Transfer 54 (2014) 8–17.

[18] M. Sathiyamoorthy, A. Chamkha, Effect of magnetic field on natural convection flow in a liquid gallium filled square cavity for linearly heated side wall (s), Int. J. Therm. Sci. 49 (9) (2010) 1856–1865.

[19] A.J. Chamkha, M.A. Ismael, Conjugate heat transfer in a porous cavity heated by a triangular thick wall, Numer. Heat Transfer, Part A: Appl. 63 (2) (2013) 144–158.

[20] N. Tatsuo, S. Mitsuhiro, K. Yuji, Natural convection heat transfer in enclosures with an off-center partition, Int. J. Heat Mass Transfer 30 (8) (1987) 1756–1758.

[21] R.S. Kaluri, R. Anandalakshmi, T. Basak, Bejan's heatline analysis of natural convection in right-angled triangular enclosures: effects of aspect-ratio and thermal boundary conditions, Int. J. Therm. Sci. 49 (9) (2010) 1576–1592.

[22] M.A. Mansour, M.A. Bakeir, A. Chamkha, Natural convection inside a C-shaped nanofluid-filled enclosure with localized heat sources, Int. J. Numer. Meth. Heat Fluid Flow 24 (8) (2014) 1954–1978.

[23] O.A. Alawi, N.A.C. Sidik, H.K. Dawood, Natural convection heat transfer in horizontal concentric annulus between outer cylinder and inner flat tube using nanofluid, Int. Commun. Heat Mass Transfer 57 (2014) 65–71.

[24] A. Baïri, H.F. Öztop, Free convection in inclined hemispherical cavities with dome faced downwards. Nu-Ra relationships for disk submitted to constant heat flux, Int. J. Heat Mass Transfer 78 (2014) 481–487.

[25] A. Baïri, E. Monier-Vinard, N. Laraqi, I. Baïri, M.N. Nguyen, C.T. Dia, Natural convection in inclined hemispherical cavities with isothermal disk and dome faced downwards. Experimental and numerical study, Appl. Therm. Eng. 73 (1) (2014) 1340–1347.

[26] A. Baïri, Nu–Ra–Fo correlations for thermal control of embarked radars contained in tilted hemispherical cavities and subjected to constant heat flux, Appl. Therm. Eng. 67 (1) (2014) 540–544.

[27] A. Baïri, J.G. de María, N. Laraqi, Transient natural convection in parallelogrammic enclosures with isothermal hot wall. Experimental and numerical study applied to on-board electronics, Appl. Therm. Eng. 30 (10) (2010) 1115–1125.

[28] S. Acharya, R. Jetli, Heat transfer due to buoyancy in a partially divided square box, Int. J. Heat Mass Transfer 33 (5) (1990) 931–942.

[29] A. Ben-Nakhi, A.J. Chamkha, Conjugate natural convection around a finned pipe in a square enclosure with internal heat generation, Int. J. Heat Mass Transfer 50 (11) (2007) 2260–2271.

[30] A. Ben-Nakhi, A.J. Chamkha, Effect of length and inclination of a thin fin on natural convection in a square enclosure, Numer. Heat Transfer 50 (4) (2006) 381–399.

[31] N.B. Cheikh, A.J. Chamkha, B.B. Beya, Effect of inclination on heat transfer and fluid flow in a finned enclosure filled with a dielectric liquid, Numer. Heat Transfer, Part A: Appl. 56 (3) (2009) 286–300.

[32] S.C. Saha, Y. Gu, Transient air flow and heat transfer in a triangular enclosure with a conducting partition, Appl. Math. Model. 38 (15) (2014) 3879–3887.
[33] S.C. Saha, M.M.K. Khan, Y. Gu, Unsteady buoyancy driven flows and heat transfer through coupled thermal boundary layers in a partitioned triangular enclosure, Int. J. Heat Mass Transfer 68 (2014) 375–382.
[34] A.N. Gent (Ed.), Engineering with Rubber, Carl Hanser Verlag, Munich, 2001.
[35] J. Donea, A. Huerta, Finite element methods for flow problems, John Wiley & Sons, 2003.
[36] O.C. Zienkiewicz, R.L. Taylor, The Finite Element Method for Solid and Structural Mechanics, Butterworth-heinemann, 2005.
[37] S.W. Churchill, Free convection in layers and enclosures. Heat exchanger design handbook, 2 (8) (1983).